CORE
Metadata, citation and similar papers at core.ac.uk
Provided by Elsevier - Publisher Connector

International Journal of Solids and Structures 51 (2014) 2729–2743

Contents lists available at ScienceDirect

International Journal of Solids and Structures

journal homepage: www.elsevier.com/locate/ijsolstr

Detecting and describing a notch in a pipe using singularities

D.K. Stoyko [a,*], N. Popplewell [a], A.H. Shah [b]

[a] Stress Engineering Services Canada, #125, 12111 - 40th Street S.E., Calgary, Alberta, T2Z 4E6, Canada
[b] Civil Engineering, University of Manitoba, 15 Gillson Street, Winnipeg, Manitoba R3T 5V6, Canada

ARTICLE INFO

Article history:
Received 3 January 2013
Received in revised form 18 December 2013
Available online 18 February 2014

Keywords:
Pipe
Notch
Singularity
Cutoff frequency
Guided waves

ABSTRACT

A hybrid Semi-Analytical Finite Element (SAFE) and standard finite element procedure is adopted to simulate ultrasonically generated waves traveling in an infinitely long steel pipe having an open, rectangular notch. Numerical illustrations indicate that dispersive guided waves can be used to locally detect and characterize such a notch. A frequency oriented approach is preferred because a problematic separation in time is circumvented when incident waves overlap their reflections from the nearby notch. The notch is discerned straightforwardly because distinctive singularities are introduced that differ from those observed at the modal cutoff frequencies in a Frequency Response Function (FRF) of a comparable but undamaged pipe. Its characterization is (suggested) demonstrated for a (non)axisymmetric notch by using several of the smallest differences in the frequencies at which the two set of singularities occur. Consequently an external stimulus that simultaneously excites more than one mode is beneficial.
© 2014 Elsevier Ltd. All rights reserved.

1. Introduction

Pipelines are used extensively to transport fluids. For example, the Alberta Energy and Utilities Board (EUB) reports (Alberta Energy and Utilities Board, 2007) that a total of 377248 km of energy related pipeline was under its jurisdiction at the end of 2005. The same source also indicates there were a total of 12848 pipeline "incidents"[1] between 1990 and 2005. About 95% of the reported incidents led to a pipeline leak or rupture. Moreover, corrosion was cited as the primary form of failure, representing approximately 70% of pipeline failures. Hidden, internal corrosion was responsible for around five times more failures than external corrosion. Although these statistics are the most currently available, they apply only to Alberta, Canada. Notwithstanding, it is clear that extensive networks of pipelines are in widespread use and they are prone to occasional failure. Given that the monetary and, less often, human costs of a pipeline failure can be extraordinarily high (Andersen and Misund, 1983), a method of inspecting pipelines is required to detect and size defects. Furthermore, the method should be nondestructive and ideally non-invasive because the infrastructure is already in service.

Ultrasonic Inspection (UI) is one of the most attractive choices for pipeline inspection. Body waves have been used for many years in a variety of UI applications, such as pulse-echo, through-transmission, resonance, etc., to perform tasks like flaw detection, thickness measurement, and characterization of a material's properties (Krautkrämer and Krautkrämer, 1977). Guided waves, on the other hand, are appealing because they can propagate over long distances, say tens of meters (Alleyne and Cawley, 1996; Rose and Quarry, 1999), and they are capable of rapidly interrogating entire structures, including otherwise inaccessible regions (Rose and Quarry, 1999). Early attempts by Mohr and Hoeller (1976) as well as Silk and Bainton (1979), for instance, of using guided waves for pipe inspection focussed on the torsional and longitudinal wave modes and considered spurious reflections as an indication of damage. More recent work as illustrated in, for example, Alleyne and Cawley (1996), the seminal work by Alleyne et al. (1998), Rose and Quarry (1999), Hay and Rose (2002), Cawley et al. (2002), Demma et al. (2004) and Ma et al. (2006) has focussed also on reflections of axisymmetric pipe modes from defects. In order to excite only these modes, or "focus" them at a desired location, special ring or "comb" transducers as well as equipment like angle beams, wedges, or time-delay, periodic linear arrays/phased arrays were employed as exemplified in Mohr and Hoeller (1976), Silk and Bainton (1979), Alleyne and Cawley (1996), Rose et al. (1996), Rose and Quarry (1999) and Mu et al. (2007). However,

* Corresponding author. Present address: Stress Engineering Services Canada, #125, 12111, 40th Street S.E., Calgary, Alberta T2Z 4E6, Canada. Tel.: +1 4032562527; fax: +1 4032562578.
E-mail addresses: Darryl.Stoyko@stress.com (D.K. Stoyko), npopple@cc.umanitoba.ca (N. Popplewell), shah@cc.umanitoba.ca (A.H. Shah).
[1] Note that incidents occurring within facilities such as satellites, batteries, or plants *are not* considered part of the pipeline system and, therefore, are not included.

http://dx.doi.org/10.1016/j.ijsolstr.2014.02.002
0020-7683/© 2014 Elsevier Ltd. All rights reserved.

the use of flexural waves (Shin and Rose, 1998, 1999; Li and Rose, 2001; Rose et al., 2003) has been infrequent because "the acoustic field is much more complicated than the case of axisymmetric modes" (Shin and Rose, 1998).

Although noticeably more effort has been expended in detecting damage in pipes (and plates) by using reflections, changes in wave speeds and dispersion curves of guided waves, cutoff frequencies have been used merely to detect thinning in plates, as in Rose and Barshinger (1998), Zhu et al. (1998) and Silva et al. (2003). Thinning was examined by exciting a guided wave mode near its cutoff frequency and monitoring the disappearance of the modal response when part of the plate's thickness was below the critical value for the mode to propagate. However, the seemingly straightforward extension to pipes does not seem to have been given. Moreover, there appears to be only one reference, Stoyko et al. (2010), employing guided wave cutoff frequencies of an undamaged pipe to *simultaneously* find its wall thickness and material properties. On the other hand, the identification of spatially decaying modes, which are introduced in a pipe by a notch and are analogous to end modes (Oliver, 1957), has not been reported.

The first objective of this paper is to demonstrate that singularities[2] distinct from an undamaged pipe's cutoff frequencies are present when a notch is introduced. These singularities are analogous, in some sense, to the end modes reported by Oliver (1957). A second objective is to describe a technique that takes advantage of these singularities to characterize the dimensions of an axisymmetric notch in a pipe. The last objective is to suggest that the extension to nonaxisymmetric and more general notch geometries is straightforward but computationally expensive.

The proposed technique to detect and characterize the dimensions of an axisymmetric notch has a number of advantages. It utilizes the classical and simplest means, i.e., a radial point load acting on the pipe's outer surface, of introducing ultrasonic energy into a pipe to simultaneously excite a number of modes. The notch may be detected by simply examining the spectral density of a measured displacement response to see if it contains the characteristic features described in Section 3.5. As frequency differences are used to infer a notch's dimensions, the need for consistent coupling is reduced somewhat compared to methods that make use of amplitude changes. A single measurement can yield sufficient information to determine an axisymmetric notch's dimensions. This attribute offers an advantage over methods that rely on the excitation of a single mode to determine a reflection coefficient, say, as at least two modes are required to *uniquely* determine even an axisymmetric notch's dimensions (Demma et al., 2004). This advantage becomes more important as the number of dimensions required to characterize a (n idealized) notch increases. Moreover, as the proposed method makes use of measurements relatively close to a notch, where waves incident and scattered by the notch may interact (in the reflected field), only modest lengths of pipe are required. Also there is no need to separate modal contributions on the basis of disparate wave speeds. However, the procedure can be applied only locally to a notch as waves are used whose amplitudes decay exponentially from a notch's boundary. The technique complements, therefore, other methods that can rapidly screen long lengths of pipe (see, for example, Alleyne et al., 1998, 2001; Rose and Quarry, 1999; Cawley et al., 2002; Mu et al., 2007).

The newly discovered singularities are demonstrated to exist first by applying the hybrid Semi-Analytical Finite Element (SAFE) in combination with a standard finite element procedure as in, for example, Rattanawangcharoen et al. (1997), Zhuang et al. (1997), Mahmoud et al. (2004) and Benmeddour et al. (2011) to axisymmetric notches in a (hollow) steel pipe. The pipe is assumed to be homogeneous, linearly elastic, isotropic, and uniformly right circular. A parametric study is undertaken subsequently in which the radial depth and axial extent of outer surface breaking, rectangular axisymmetric notches are varied independently. The results are used to illustrate how the frequency difference between the new singularities and an undamaged pipe's cutoff frequencies can be used to detect a notch and determine its size. Notwithstanding that internal corrosion occurs more often than external corrosion, solely outer surface breaking notches are considered because the simulations presented here can be partially corroborated by existing experimental data (Alleyne et al., 1998). The examples suggest that *almost*[3] any set, which contains a sufficient number of accurate frequency differences, will give the same inverse solution. Note, however, that uniqueness is not proven, it is merely suggested. The modes may be selected generally but usually on the basis of ease of experimental implementation.[4] The extension to nonaxisymmetric notches is suggested by showing that the singularities exist also in the more general three-dimensional case. Then conclusions and closing remarks are made. An appendix which provides comparisons between the predictions that arise from the simulations and other's, independently obtained experimental data (Alleyne et al., 1998) concludes the paper.

2. Hybrid SAFE and standard finite element

2.1. Overview of hybrid wave function-standard finite element approach

A hybrid wave function-standard finite element approach can be used to model wave scattering by a nonhomogeneity in an otherwise continuous waveguide. The methodology employs a conventional finite element description to model the displacement field in a region completely enclosing the nonhomogeneity. On the other hand, the displacement field in the remainder of the waveguide is described in terms of a modal expansion of the wave functions of the undamaged waveguide. An incident wave field is generated outside the conventional finite element region. Waves are scattered by the nonhomogeneity. The scattered wave field is obtained by enforcing continuity (displacements and stresses/nodal forces) between the finite element and wave function expansion regions. In a hybrid SAFE and standard finite element model, the wave functions are obtained by applying the SAFE methodology to the waveguide, rather than using a method that provides "exact" wave functions.

Fig. 1(a) shows standard orthographic views of a pipe having a nonaxisymmetric, outer surface breaking notch. The notch takes the role of the nonhomogeneity when applying the hybrid wave function-standard finite element approach. It can be seen from Fig. 1(a) that the notch may be bounded by the planes $z = 0$ and $z = -2z_{FE}$, which are used to demarcate the axial extents of the finite element region. The motion in pipe outside the finite element region is described in terms of a wave function expansion of the undamaged pipe's normal modes. An incident wave field is generated by the transient input excitation, shown as a radial point force in the figure, applied in the $z = z_L$ plane. Wave scattering by the notch will give rise to a combined incident and reflected

[2] The term singularity is used here to indicate a frequency at which a displacement response of a given guided wave mode becomes very large and behaves similarly to a resonant frequency of an undamped single degree of freedom oscillator.

[3] The T(0,1), L(0,1), and F(1,1) modes, for example, are excluded because they always have a zero singularity frequency for a simple homogeneous, isotropic pipe and, hence, they are unsuitable.

[4] The F(3,2) and F(11,2) modes, say, have no radial displacement component at their respective cutoff frequencies. Consequently, neither mode would be detectable at (or near) their cutoff frequencies by a transducer which measures a solely radial displacement.

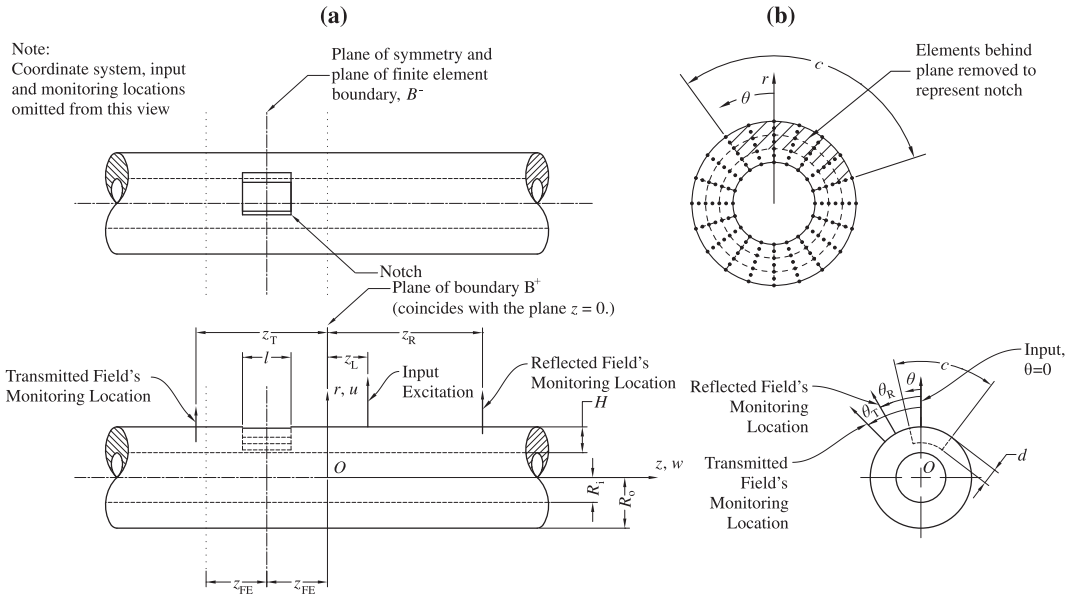

Fig. 1. Illustrating (a) a nonaxisymmetrically notched pipe and (b) the finite element nodal points on boundary B^+ which is located at $z = 0$. Point "O" is the origin of the cylindrical coordinate system.

(transmitted) wave field in the wave function expansion region corresponding to $z \geqslant 0$ ($z \leqslant -2z_{FE}$) in the configuration shown. As illustrated, the notched pipe shown is symmetric[5] about the plane $z = -z_{FE}$ which corresponds to the finite element boundary B^-. Computationally advantageous use is made of this symmetry by decomposing the input excitation into the sum of a pair of forces that are symmetric and antisymmetric about the plane $z = -z_{FE}$, as illustrated in Fig. 2.

Then boundary conditions appropriate for symmetric and antisymmetric loadings can be applied to the finite element boundary B^-. More specifically, for (anti) symmetric loading, the displacement in the (r and θ) z direction(s), as well stress (σ_{zz}) σ_{rz} and $\sigma_{\theta z}$ vanish on boundary B^-. This standard finite element technique is described more fully in Cook (1981). Moreover, as a consequence of this procedure, the amplitude of the scattered waves need be computed only for $z \geqslant 0$, i.e., the reflected field, because the wave field in the transmitted field can be obtained from the reflected field by applying symmetric and antisymmetric arguments. From Fig. 2 it can be seen that the reflected wave are given by the sum of the symmetric and antisymmetric solutions, while the transmitted wave field is given by their difference.

Three components are required to apply the hybrid wave function-standard finite element technique. They are: (i) the wave functions of the undamaged waveguide, (ii) a finite element description of the region enclosing the defect, and (iii) a method of enforcing continuity conditions between the first two components. Each component is described briefly now.

2.2. SAFE modeling for pipes

The finite element procedure for representing the wave motions through a pipe's wall, combined with a separation of variables strategy for the other coordinates (i.e., a Semi-Analytical Finite

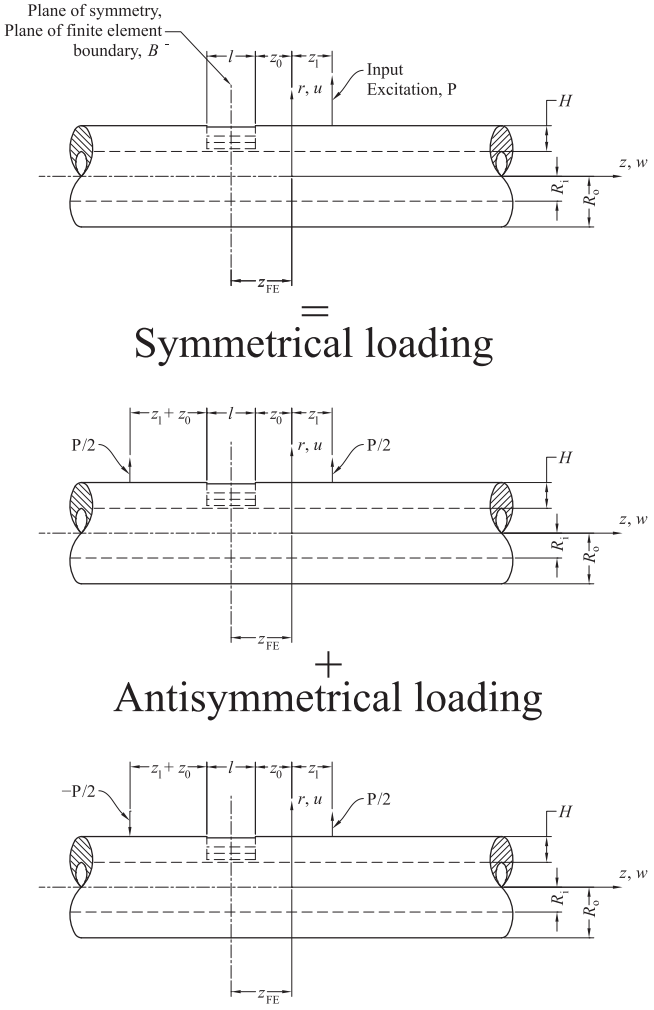

Fig. 2. Illustrating the decomposition of a point force, **P**, into a superposition of two symmetrical and antisymmetrical forces, **P**/2, about the plane $z = -z_{FE}$.

[5] Symmetry is not required to employ the hybrid wave function-standard finite element technique. Geometries that do not possess a plane of symmetry can be accommodated by enforcing continuity conditions between the finite element region and wave guide on two cross sections, rather than the single plane employed here. However, the computational effort is increased.

Element (SAFE) approach), seems to have been reported first for pipes (cylinders) by Nelson et al. (1971). Further enhancements include the modeling of laminations, as well as anisotropic, electrical, thermal, and viscoelastic effects. Contributions are described in, for example, Huang and Dong (1984), Rattanawangcharoen et al. (1992), Zhuang et al. (1999), Huang and Dong (2001a,b), Bai et al. (2004, 2011), Marzani (2008) and Chitikireddy et al. (2011). Consequently only an overview of the SAFE procedure is given.

The SAFE formulation, detailed exhaustively in Zhuang et al. (1999), provides an easily applied and accurate numerical model by which the Green's and wave functions of a more general laminated pipe may be computed for a harmonic excitation having circular frequency ω. The frequency ω may be chosen arbitrarily so that, most importantly, an arbitrarily fine frequency resolution may be achieved computationally. This general methodology is adapted here, with straightforward simplifications, to compute the wave functions of a homogeneous, isotropic pipe subjected to a transient excitation. Note that the frequency resolution from an initial time integration and later Discrete Fourier Transform (DFT) is limited as a consequence of the transient's short duration. The transient excitation is decomposed into an infinite number of discrete frequency components by using a Fourier transform. Each frequency component of a *point force* is approximated by using a "narrow" pulse having a uniform amplitude of $(2r_0\theta_0)^{-1}$ over a circumferential distance $2r_0\theta_0$ to circumvent convergence difficulties. The r_0 is the radial coordinate where the point-like force is applied, whereas θ_0 is the circumferential angle over which the pulse extends. This narrow pulse is represented, in turn, by employing a Fourier series, in the circumferential direction, of "ring-like" loads having separable spatial and time, t, variations.

The pipe is discretised by using N layers through its thickness. The layers are taken to have identical thicknesses here. Each layer corresponds to a one-dimensional finite element in the pipe's radial direction for which a quadratic displacement interpolation function is assumed. A finite element approach is applied, layer by layer, in SAFE to approximate the elastic equations of motion. The displacement is represented, like the excitation, by a Fourier series in the circumferential coordinate.

The Fourier series describing the excitation and displacement are substituted into approximate equations of motion obtained from Hamilton's principle. The result is transformed into the wave-number domain by applying the Fourier integral transform. Then the nth circumferential harmonic (wave number[6]) takes the form of a quadratic eigensystem which is linearized for the special case when no excitation is applied. The resulting eigenvalues,[7] k_{nm}, and (right) eigenvectors, $\boldsymbol{\phi}^{\mathrm{R}}_{nm}$, of this eigensystem are the approximate axial wave numbers and modes shapes through the thickness, respectively, for the nth circumferential harmonic. Both the displacement (response) and excitation, for the nth circumferential harmonic, are expanded into a series of the normal modes (wave functions) of the linearized eigensystem. A displacement is obtained, for the nth circumferential wave-number and those axial cross sections having positive or negative z, by linearly superimposing the appropriate admissible $6N+3$ right eigenvector solutions (Zhuang et al., 1999). Applying first the inverse Fourier transform to this sum, and then Cauchy's residue theorem, produces the nth circumferential mode of the displacement. A linear superposition of the circumferential harmonics gives the displacement for a harmonic component of the excitation. The total displacement produced by a multi-frequency excitation is found by linearly superimposing the displacements caused by each individual frequency component. See Stoyko (2005, 2012) for further details.

2.3. Finite element idealization

The finite element method is a well understood tool that is in common use. Therefore, only an outline pertinent to implementing the hybrid wave function-standard finite element technique is provided.

Hamilton's principle is applied straightforwardly in the finite element region immediately surrounding the notch to give

$$\mathbf{S}\mathbf{q} = \mathbf{P} \tag{1}$$

where

$$\mathbf{S} = \mathbf{K}_{\mathrm{I}} - \omega^2\mathbf{M}_{\mathrm{I}}. \tag{2}$$

The $\mathbf{q}$ and $\mathbf{P}$ are the assembled vectors of nodal displacements and forces, respectively, for the finite element region. The $\mathbf{K}_{\mathrm{I}}$ and $\mathbf{M}_{\mathrm{I}}$ in Eq. (2) are the assembled stiffness and mass matrices, respectively, of the finite element region, and ω is an angular frequency component of the excitation. The subscript I has been applied to the mass and stiffness matrices of the (inner) finite element region to distinguish them from the corresponding matrices used in the SAFE procedure.

To represent a notch, elements are simply removed from the finite element mesh when forming $\mathbf{K}_{\mathrm{I}}$ and $\mathbf{M}_{\mathrm{I}}$. See also Fig. 1(b). It is well understood (Owen and Fawkes, 1983; Alleyne et al., 1998; Bai et al., 2001; Benmeddour et al., 2011) that singularities in the stress field that occur at the notch's corners are not described accurately by this method.[8] However, the far field behavior is modeled with sufficient accuracy to be meaningful (Owen and Fawkes, 1983; Alleyne et al., 1998; Bai et al., 2001; Benmeddour et al., 2011).

A series of condensations is performed now in order to eliminate degrees of freedom associated with nodes interior to the finite element region, leaving only degrees of freedom on the boundary that interfaces the wave function and finite element regions. The dynamic stiffness matrix, $\mathbf{S}$, is modified at each stage of this process. Each modification to $\mathbf{S}$ is indicated by embellishing the previous dynamic stiffness matrix with a leading, sequentially increasing numerical subscript.

Eq. (1) can be partitioned as

$$\begin{bmatrix} \mathbf{S}_{\mathrm{II}} & \mathbf{S}_{\mathrm{IB}} \\ \mathbf{S}_{\mathrm{BI}} & \mathbf{S}_{\mathrm{BB}} \end{bmatrix} \begin{Bmatrix} \mathbf{q}_{\mathrm{I}} \\ \mathbf{q}_{\mathrm{B}} \end{Bmatrix} = \begin{Bmatrix} \mathbf{P}_{\mathrm{I}} \\ \mathbf{P}_{\mathrm{B}} \end{Bmatrix}, \tag{3}$$

where subscript I (B) refers to a node of the finite element region that is inside (on the boundaries [B^+ or B^-]) of the finite element region. (Boundaries B^+ and B^- correspond to the planes $z=0$ and $z=-z_{\mathrm{FE}}$, respectively.) Assuming that no external load is located in the finite element region (i.e., all loads are applied to B^+ or B^- of the finite element region) gives $\mathbf{P}_{\mathrm{I}} = \mathbf{0}$. The displacements of the internal nodes may be condensed from Eq. (3) to give

$${}_1\mathbf{S}\mathbf{q}_{\mathrm{B}} = \mathbf{P}_{\mathrm{B}}, \tag{4}$$

where

$${}_1\mathbf{S} = \left(-\mathbf{S}_{\mathrm{BI}}\mathbf{S}_{\mathrm{II}}^{-1}\mathbf{S}_{\mathrm{IB}} + \mathbf{S}_{\mathrm{BB}}\right). \tag{5}$$

Eq. (5) contains only quantities related to nodes on the boundaries of the finite element region. Eq. (4) can be partitioned as

[6] The circumferential wave numbers of a right circular pipe can take only integer values due to the requirement that the displacement field should be single valued.

[7] The index m is an integer value that is used to indicate the mth axial mode corresponding to the nth circumferential wave number. Modes are labeled using the standard convention described in Silk and Bainton (1979).

[8] Crack-tip elements, having their "side nodes at quarter points of their respective sides", (Cook, 1981) could have been used to improve the near field accuracy. However, these elements were not used for simplicity.

$$\begin{bmatrix} {}_1\mathbf{S}_{--} & {}_1\mathbf{S}_{-+} \\ {}_1\mathbf{S}_{+-} & {}_1\mathbf{S}_{++} \end{bmatrix} \begin{Bmatrix} \mathbf{q}_- \\ \mathbf{q}_+ \end{Bmatrix} = \begin{Bmatrix} \mathbf{P}_- \\ \mathbf{P}_+ \end{Bmatrix}, \tag{6}$$

in which subscripts − and + refer to a node of the finite element region that is on boundary B^- or B^+.

Advantage is taken now of the symmetry of the notched pipe about the plane $z = -z_{FE}$ to eliminate quantities associated with the boundary B^-. As stated previously, the input loading is decomposed into the sum of symmetric and antisymmetric loadings about the plane $z = -z_{FE}$. It is well known, see for example Cook (1981), that for (anti) symmetric loadings, the displacement in the (r and θ) z direction(s), as well stress (σ_{zz}) σ_{rz} and $\sigma_{\theta z}$ vanish on B^-. The disappearance of a stress gives a corresponding null (consistent) nodal force. (Nodal forces f_r, f_θ, f_z correspond to the σ_{rz}, $\sigma_{\theta z}$, σ_{zz} stress components, respectively.) The assembled displacement and force vectors for the boundary B^-, $\mathbf{q}_-$ and $\mathbf{P}_-$, can be written therefore for symmetric loadings as

$$\mathbf{q}_{s-} = [\mathbf{u}_{sr-} \quad \mathbf{u}_{s\theta-} \quad \mathbf{0}]^T \quad \text{and} \quad \mathbf{P}_{s-} = [\mathbf{0} \quad \mathbf{0} \quad \mathbf{f}_{sz-}]^T \tag{7a}$$

and for antisymmetric loadings as

$$\mathbf{q}_{a-} = [\mathbf{0} \quad \mathbf{0} \quad \mathbf{u}_{az-}]^T \quad \text{and} \quad \mathbf{P}_{a-} = [\mathbf{f}_{ar-} \quad \mathbf{f}_{a\theta-} \quad \mathbf{0}]^T, \tag{7b}$$

where subscript (a) s denotes the (anti) symmetric loading. Note, from Eq. (7), that where a displacement is known on B^-, the corresponding (reaction) force is unknown. These forces can be determined, as in any displacement-based finite element procedure, after the displacements throughout the finite element region have been found. As the amplitudes of the scattered waves are ultimately the desired quantities, these unknown reaction forces are left undetermined (to reduce the number of floating point operations performed) as they are not presently of interest. For both the symmetric and antisymmetric cases, appropriate rows and columns of ${}_1\mathbf{S}_{--}$, ${}_1\mathbf{S}_{-+}$, and ${}_1\mathbf{S}_{+-}$ may be deleted by considering the zero displacements on B^- and ignoring the corresponding unknown reaction forces. This neglect allows Eq. (6) to be simplified, for both cases, to

$$\begin{bmatrix} {}_2\mathbf{S}_{--} & {}_2\mathbf{S}_{-+} \\ {}_2\mathbf{S}_{+-} & {}_1\mathbf{S}_{++} \end{bmatrix} \begin{Bmatrix} {}_2\mathbf{q}_- \\ \mathbf{q}_+ \end{Bmatrix} = \begin{Bmatrix} \mathbf{0} \\ \mathbf{P}_+ \end{Bmatrix}. \tag{8}$$

Note that ${}_1\mathbf{S}_{++}$, $\mathbf{q}_+$, and $\mathbf{P}_+$ remain unchanged in this process. In a similar manner to how the displacements of the internal nodes are eliminated from Eq. (3), ${}_2\mathbf{q}_-$ can be eliminated from Eq. (8) to give

$${}_3\mathbf{S}\mathbf{q}_+ = \mathbf{P}_+, \tag{9}$$

where

$${}_3\mathbf{S} = \left(-{}_2\mathbf{S}_{+-} \cdot {}_2\mathbf{S}_{--}^{-1} \cdot {}_2\mathbf{S}_{-+} + {}_1\mathbf{S}_{++}\right). \tag{10}$$

Eq. (9) contains a known dynamic stiffness matrix, ${}_3\mathbf{S}$, and, as yet, unknown finite element nodal displacements and forces on boundary B^+. These unknown displacements and forces are written, in the upcoming Section 2.4, in terms of the undamaged pipe's wave functions for two cases. The first case is when the notch[9] is axisymmetric, i.e., c in Fig. 1(b) is 360° (2π); the second case is when c is less than 360° (2π).

2.4. Interface between the wave function and finite element regions

A single incident wave mode of unit magnitude that is incident on the plane $z = 0$ is considered for simplicity. The scattering caused by an arbitrary incident wave field may be constructed by appropriately scaling and superimposing[10] the scattered wave fields calculated for all the modes present in the incident field. For the sake of discussion, let the incident wave be time harmonic with circular frequency ω and have a circumferential wave number n_{in}, with an axial wave number $k_{n_{in}m_{in}}$. Note that only modes having a non-positive imaginary component to their axial wave number are admissible in the incident field for the configuration shown in Fig. 1. This restriction is due to the radiation condition that requires the displacement field to remain bounded at $z = \pm\infty$.

2.4.1. Axisymmetric notches

It is appropriate to use axisymmetric elements in the finite element region when the notch is axisymmetric. Then the finite element nodal points on the boundary B^+, as shown in Fig. 1(b), lie on the single radial line $\theta = 0$. Note that, because the wavefunction expansion regions and the finite element region are axisymmetric, the circumferential wave number of the scattered waves is required to be identical[11] to that of the incident waves. See, for example, Cook (1981).

The finite element region is chosen in the axisymmetric case such that its axial boundaries corresponds to those of the notch, i.e., the finite element region is bounded by the planes $z = -l$ and $z = 0$. The plane of symmetry is then $z = -l/2$, and $2z_{FE} = l$. This choice simultaneously simplifies the computations and reduces the number of finite elements used in the idealization.

Using modal superposition, the displacements of the reflected wave field caused by the incident wave can be written at the finite element nodal points along the radial line $\theta = 0$ in the form

$$\mathbf{q}_+^s = \sum_{m_s=1}^{6N+3} A_{n_s m_s} \boldsymbol{\phi}_{n_s m_s}^R \exp(\mathrm{j} k_{n_s m_s} z) = \mathbf{G}\mathbf{A}, \tag{11}$$

where the superscript and sub, subscript s indicates the scattered wave field and $A_{n_s m_s}$, $\boldsymbol{\phi}_{n_s m_s}^R$, and $n_s = n_{in}$ and $k_{n_s m_s}$ are the amplitude, mode shape, and circumferential and axial wave numbers, respectively, of the $n_s m_s^{th}$ scattered mode. (Note that only modes having non-negative, imaginary wave number components are admissible in the reflected wave field.) As the displacements are evaluated at $z = 0$, the exponential term in Eq. (11) takes the value of unity and $\mathbf{G}$ becomes a matrix containing the mode shapes of the reflected wave field. On the other hand, continuities of the nodal forces and displacements on boundary B^+ require that

$$\mathbf{q}_+ = \mathbf{q}_+^{in} + \mathbf{q}_+^s \tag{12a}$$

and

$$\mathbf{P}_+ = \mathbf{f}_+^{in} + \mathbf{f}_+^s, \tag{12b}$$

where the superscript "in" indicates a quantity associated with the incident wave field. The displacement of the incident wave field at the finite element nodal points along the radial line $\theta = 0$ is simply the mode shape of the incident mode. The (consistent) force vector at these points can be obtained, for the incident wave field, $\mathbf{f}_+^{in}$, by expressing the modal stresses in terms of the displacement wave functions and then integrating the product of these stresses and the finite element shape functions over the surface of each finite element. The force vector at these same points may be found similarly for the reflected field so that $\mathbf{f}_+^s$ may be expressed as

$$\mathbf{f}_+^s = \mathbf{F}_s\mathbf{A}, \tag{13}$$

where $\mathbf{F}_s$ is a matrix that "maps" vector $\mathbf{A}$ of the scattered wave amplitudes into the required nodal forces.

[9] A notch may have a depth, d, which is zero and represents an undamaged pipe. This important case is considered in the transparency check discussed later.

[10] Linearity is assumed implicitly throughout.

[11] This is true when isotropy is assumed. It is not the case for general anisotropy. See, for example, Cook (1981).

Eqs. (9) and (12) lead to

$$ {}_3\mathbf{S}\left(\mathbf{q}_+^{\text{in}} + \mathbf{q}_+^{\text{s}}\right) = \mathbf{f}_+^{\text{in}} + \mathbf{f}_+^{\text{s}}, \tag{14} $$

which, when rearranged, gives

$$ {}_3\mathbf{S}\mathbf{q}_+^{\text{s}} - \mathbf{f}_+^{\text{s}} = \mathbf{f}_+^{\text{in}} - {}_3\mathbf{S}\mathbf{q}_+^{\text{in}}. \tag{15} $$

Substituting Eqs. (11) and (13) into Eq. (15) gives

$$ ({}_3\mathbf{S}\mathbf{G} - \mathbf{F}_{\text{s}})\mathbf{A} = \mathbf{f}_+^{\text{in}} - {}_3\mathbf{S}\mathbf{q}_+^{\text{in}}. \tag{16} $$

Furthermore, when all the approximate modes are retained in the modal expansion, as assumed here, the number of modes equals the order of $({}_3\mathbf{S}\mathbf{G} - \mathbf{F}_{\text{s}})$. Moreover, $({}_3\mathbf{S}\mathbf{G} - \mathbf{F}_{\text{s}})$ is square and invertible so that the amplitudes of the scattered waves can be recovered as

$$ \mathbf{A} = ({}_3\mathbf{S}\mathbf{G} - \mathbf{F}_{\text{s}})^{-1}\left(\mathbf{f}_+^{\text{in}} - {}_3\mathbf{S}\mathbf{q}_+^{\text{in}}\right). \tag{17} $$

Eq. (17) must be evaluated for both the symmetric and antisymmetric components of the load, by changing the boundary conditions on B^-, in order to recover their combined effects. At any location, the reflected ($z \geqslant 0$) and transmitted ($z \leqslant -2z_{\text{FE}}$) wave amplitudes for the $n_{\text{s}}m_{\text{s}}^{\text{th}}$ scattered mode, $R_{n_{\text{s}}m_{\text{s}}}$ and $T_{n_{\text{s}}m_{\text{s}}}$ respectively, due to a given incident mode, are given by

$$ R_{n_{\text{s}}m_{\text{s}}} = \left(A^{\text{s}}_{n_{\text{s}}m_{\text{s}}} + A^{\text{a}}_{n_{\text{s}}m_{\text{s}}}\right)/2 \tag{18a} $$

and

$$ T_{n_{\text{s}}m_{\text{s}}} = \left(A^{\text{s}}_{n_{\text{s}}m_{\text{s}}} - A^{\text{a}}_{n_{\text{s}}m_{\text{s}}}\right)/2. \tag{18b} $$

The $A_{n_{\text{s}}m_{\text{s}}}$ is the $n_{\text{s}}m_{\text{s}}^{\text{th}}$ scattered wave amplitude and superscript (a) s denotes the solution corresponding to the (anti) symmetric boundary conditions. $R_{n_{\text{s}}m_{\text{s}}}$ and $T_{n_{\text{s}}m_{\text{s}}}$ represent *normalized* reflection and transmission coefficients, respectively, because they are calculated by assuming a *single incident mode having a unit amplitude*.[12] Moreover, the $R_{n_{\text{s}}m_{\text{s}}}$ and $T_{n_{\text{s}}m_{\text{s}}}$ represent the amplitudes of the scattered waves at the planes $z = 0$ and $z = -2z_{\text{FE}}$, respectively.

2.4.2. Nonaxisymmetric notches

The nonaxisymmetric case is similar to, but somewhat more complicated than, the axisymmetric case. Only relevant differences are described.

The finite element region is chosen in the nonaxisymmetric case so that at least one complete "ring" of finite elements (that mate "perfectly" with the undamaged sections of pipe) extends, in both the positive and negative axial directions, beyond the notch's axial extent. This choice avoids the use of "mixed" continuity conditions between the finite element and wave function expansion regions (Bai et al., 2001).

Three-dimensional elements are required to describe the displacement field in the finite element region when the notch is nonaxisymmetric. The finite element nodal points on the boundary B^+ are arranged around this entire boundary, as shown in Fig. 1(b). All the circumferential wave numbers used in the modal expansion participate, in principle, in the reflected displacement field now that the finite element region is no longer axisymmetric, even though a single incident wave is assumed.

Using modal superposition, the displacements of the reflected wave field can be written at the finite element nodal points in the form

$$ \mathbf{q}_+^{\text{s}} = \sum_{n_{\text{s}}=n_{\min}}^{n_{\max}} \sum_{m_{\text{s}}=1}^{6N+3} A_{n_{\text{s}}m_{\text{s}}} \boldsymbol{\phi}^{\text{R}}_{n_{\text{s}}m_{\text{s}}} \exp(\text{j}k_{n_{\text{s}}m_{\text{s}}}z)\exp(\text{j}n_{\text{s}}\theta) = \mathbf{G}\mathbf{A}, \tag{19} $$

where $n_{\min}$ and $n_{\max}$ are the minimum and maximum circumferential wave numbers, respectively, employed in the modal expansion of the reflected field. (The remaining nomenclature has been defined in Section 2.4.1.) As the displacements are evaluated at $z = 0$, the first exponential term in Eq. (19) takes the value of unity. As before, the $\mathbf{G}$ in Eq. (19) matrix "maps" the reflected wave amplitudes into the required nodal displacements. This $\mathbf{G}$ matrix is somewhat more involved, however, than that appearing in Eq. (11) because, in addition to containing the mode shapes of the reflected wave field, circumferential variations must be also included.

Eqs. (12)–(14) remain applicable in the three-dimensional case. The procedure to recover the scattered wave's amplitudes must be modified, however, because $({}_3\mathbf{S}\mathbf{G} - \mathbf{F}_{\text{s}})$ is not generally square and, therefore, not invertible. The principle of virtual work is applied next to recover the amplitudes of the scattered waves.

No real or virtual work is performed on the plane of symmetry, $z = -z_{\text{FE}}$, because, at each nodal point on this boundary, all the nodal forces in each coordinate direction, or their complementary displacement components, are identically zero. Therefore, the virtual work done on the finite element region, $\delta\mathcal{E}_{\text{virt}}$, can be expressed as

$$ \delta\mathcal{E}_{\text{virt}} = \frac{1}{2}\left(\overline{\delta\mathbf{q}_+}^{\text{T}}\mathbf{P}_+ + \delta\mathbf{q}_+^{\text{T}}\overline{\mathbf{P}_+}\right), \tag{20} $$

where an over bar indicates complex conjugation and δ indicates the first variation which vanishes for equilibrium. By performing this variation, the resulting equation

$$ \overline{\delta\mathbf{q}_+}^{\text{T}}\mathbf{P}_+ = 0 \tag{21} $$

can be shown to be sufficient for the virtual work to be stationary. The $\overline{\delta\mathbf{q}_+}^{\text{T}}$ can be determined, by using Eq. (12a), to be

$$ \overline{\delta\mathbf{q}_+}^{\text{T}} = \overline{\delta\mathbf{q}_+^{\text{in}}}^{\text{T}} + \overline{\delta\mathbf{q}_+^{\text{s}}}^{\text{T}}. \tag{22} $$

The displacements of the incident wave field are prescribed at the finite elements' nodal points and, therefore, have no variation, i.e., $\overline{\delta\mathbf{q}_+^{\text{in}}}^{\text{T}} = \mathbf{0}$. Consequently, Eq. (22) reduces to

$$ \overline{\delta\mathbf{q}_+}^{\text{T}} = \overline{\delta\mathbf{q}_+^{\text{s}}}^{\text{T}}. \tag{23} $$

Substituting Eq. (19) into Eq. (23) and noting that $\mathbf{G}$ is constant leads to

$$ \overline{\delta\mathbf{q}_+}^{\text{T}} = \overline{\delta\mathbf{A}}^{\text{T}}\overline{\mathbf{G}}^{\text{T}}. \tag{24} $$

Applying the principle of virtual work to Eq. (14) produces

$$ \begin{aligned} \overline{\delta\mathbf{A}}^{\text{T}}\overline{\mathbf{G}}^{\text{T}}{}_3\mathbf{S}\mathbf{q}_+ &= \overline{\delta\mathbf{A}}^{\text{T}}\overline{\mathbf{G}}^{\text{T}}\mathbf{P}_+ = \overline{\delta\mathbf{A}}^{\text{T}}\overline{\mathbf{G}}^{\text{T}}{}_3\mathbf{S}\left(\mathbf{q}_+^{\text{in}} + \mathbf{q}_+^{\text{s}}\right) \\ &= \overline{\delta\mathbf{A}}^{\text{T}}\overline{\mathbf{G}}^{\text{T}}\left(\mathbf{f}_+^{\text{in}} + \mathbf{f}_+^{\text{s}}\right) = 0, \end{aligned} \tag{25} $$

when Eqs. (21) and (24) are utilized. Eq. (25) implies that

$$ \overline{\mathbf{G}}^{\text{T}}{}_3\mathbf{S}\left(\mathbf{q}_+^{\text{in}} + \mathbf{q}_+^{\text{s}}\right) = \mathbf{0} \tag{26a} $$

and

$$ \overline{\mathbf{G}}^{\text{T}}\left(\mathbf{f}_+^{\text{in}} + \mathbf{f}_+^{\text{s}}\right) = \mathbf{0}, \tag{26b} $$

because $\overline{\delta\mathbf{A}}^{\text{T}}$ is arbitrary. Setting Eqs. (26a) and (26b) equal leads, after rearrangements, to

$$ \overline{\mathbf{G}}^{\text{T}}\left({}_3\mathbf{S}\mathbf{q}_+^{\text{in}} - \mathbf{f}_+^{\text{in}}\right) = \overline{\mathbf{G}}^{\text{T}}\left(\mathbf{f}_+^{\text{s}} - {}_3\mathbf{S}\mathbf{q}_+^{\text{s}}\right). \tag{27} $$

The right side of Eq. (27) can be expressed in terms of the scattered wave amplitudes by using Eqs. (13) and (19). Hence,

$$ \overline{\mathbf{G}}^{\text{T}}\left({}_3\mathbf{S}\mathbf{q}_+^{\text{in}} - \mathbf{f}_+^{\text{in}}\right) = \overline{\mathbf{G}}^{\text{T}}(\mathbf{F}_{\text{s}}\mathbf{A} - {}_3\mathbf{S}\mathbf{G}\mathbf{A}) = \overline{\mathbf{G}}^{\text{T}}(\mathbf{F}_{\text{s}} - {}_3\mathbf{S}\mathbf{G})\mathbf{A}. \tag{28} $$

The matrix product $\overline{\mathbf{G}}^{\text{T}}(\mathbf{F}_{\text{s}} - {}_3\mathbf{S}\mathbf{G})$ is square and invertible so that

$$ \mathbf{A} = \left[\overline{\mathbf{G}}^{\text{T}}(\mathbf{F}_{\text{s}} - {}_3\mathbf{S}\mathbf{G})\right]^{-1}\overline{\mathbf{G}}^{\text{T}}\left({}_3\mathbf{S}\mathbf{q}_+^{\text{in}} - \mathbf{f}_+^{\text{in}}\right). \tag{29} $$

[12] Note that the magnitudes of $R_{n_{\text{s}}m_{\text{s}}}$ and $T_{n_{\text{s}}m_{\text{s}}}$ depend on the scaling of the mode shapes; all mode shapes are scaled here to have a vector norm magnitude of unity.

As for the axisymmetric case, Eq. (29) must be evaluated for both the symmetric and antisymmetric boundary conditions in order to recover the combined effect. Then the ensuing reflected and transmitted wave amplitudes may be found by using Eq. (18).

3. Illustrative examples

3.1. Overview

Having provided an overview of the hybrid-SAFE technique for both axisymmetric and nonaxisymmetric wave scatterers in Section 2, it is applied in this section to model wave scattering from two illustrative rectangular notches in an otherwise blemish free pipe. The first notch is axisymmetric, while the second is nonaxisymmetric. Both notches are outer surface breaking and have finite radial depths and axial extents. Note that the accuracy of the software has been checked by applying transparency and energy balance considerations (Stoyko, 2012). Moreover, comparisons between available, but limited, experimental data (Alleyne et al., 1998) and the predictions from the software produce results that are generally in good agreement. The properties assumed for the undamaged pipe and excitation pulse are described first. Then an overview is given of the SAFE analysis which is performed to recover approximate wave functions for the pipe. Finally results are given for the wave scattering from the two illustrative notches.

3.2. Undamaged pipe's description

The undamaged pipe, whose properties are summarised in Table 1, is assumed to be uniform, hollow, right circular, homogeneous, and isotropic. These properties are representative for an undamaged, seamless, Schedule 40, 80 mm Diamètre Nominal (DN), steel pipe. Moreover, the properties are essentially identical to the pipe examined experimentally by Alleyne et al. (1998).

3.3. Excitation's form

The function, $p(t)$, which describes the temporal variation of the applied force is idealized as the commonly used Gaussian modulated sine wave that has the form

$$p(t) = \begin{cases} 0, & t < 0, \\ A\exp\left[-a(st-\tau)^2\right]\sin(s\omega_0 t), & t \geqslant 0, \end{cases} \tag{30}$$

where A is an amplitude, a determines the rate of decay of the pulse, s serves to "scale" time, τ centers the pulse in time, t, and ω_0 sets the center frequency of the sine wave. The constant a, s, τ, and ω_0 are taken invariably here to be

$$a = 2.29595 \times 10^{10}\ \mathrm{s}^{-2}, \tag{31a}$$

$$s = 0.28, \tag{31b}$$

$$\tau = 1.4 \times 10^{-5}\ \mathrm{s} \tag{31c}$$

Table 1
Properties assigned to the undamaged steel pipe.

Property	Assigned value
Density, ρ, kg m^{-3}	7932
Outer diameter, D_o, mm	88.8
Wall thickness, H, mm	5.59
Mean radius, R, mm	41.60
Thickness to mean radius ratio, (H/R)	0.134
Young's modulus, E, GPa	216.9
Lamé constant (shear modulus), μ (G), GPa	84.3
Lamé constant, λ, GPa	113.2
Ratio of Lamé constants, (λ/μ)	1.34
Poisson's ratio, ν	0.286

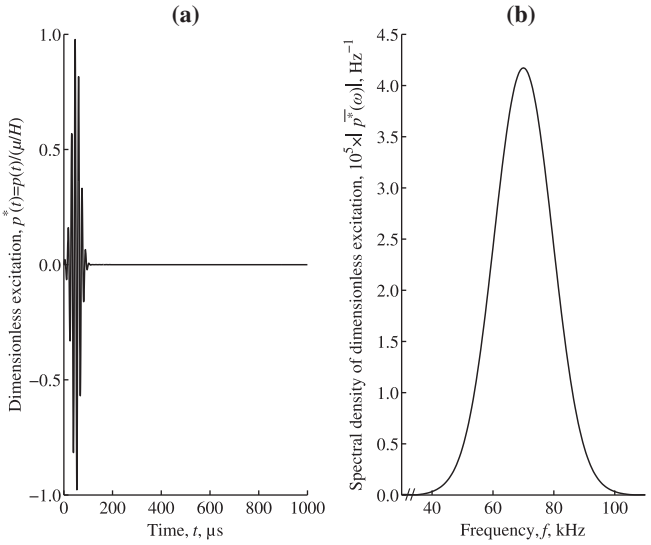

Fig. 3. Applied excitation in (a) time and (b) frequency.

and

$$\omega_0 = (5 \times 10^5)\pi\ \mathrm{rad/s}. \tag{31d}$$

Moreover, the (body force) amplitude is taken always as $A = (\mu/H)$, where μ is the pipe's shear modulus (Lamé constant) and H is its wall thickness, which corresponds to a dimensionless unit amplitude.[13] The previously described pulse is smooth (i.e., differentiable) in both time and frequency and, with the chosen constants, simultaneously has a relatively short duration and narrow frequency bandwidth. The short duration is useful for "time of flight" applications; the narrow band frequency character allows the Fourier transform to be approximated by assuming a finite bandwidth. For the given constants, the force has a 70 kHz center frequency and over 99% of its energy is contained within the 35 to 107 kHz bandwidth. Therefore the Fourier integral transform of $p(t)$, $\overline{p}(\omega)$, may be assumed reasonably to be contained within this finite bandwidth. The resulting forms of $p(t)$ and $|\overline{p}(\omega)|$ are illustrated in Fig. 3.

3.4. Approximate wave functions from SAFE

In determining approximate wave functions by using SAFE, ten identically thick finite elements are used to uniformly discretise the pipe's wall thickness, H. The circumferential angle, $2\theta_0$, over which the spatial pulse approximates the Dirac delta function, is taken to be 0.002 radians (0.1°). Circumferential wavenumbers n, from 0 to ±16, and all the $6N + 3$ corresponding axial modes, having wavenumbers k_{nm} and mode shapes $\boldsymbol{\Phi}^{\mathrm{R}}_{nm}$, are incorporated into the wave scattering computations. Numerical and experimental investigations of the undamaged pipe's displacement response may be found in Stoyko (2005, 2012) and Stoyko et al. (2010).

3.5. Axisymmetric notch

An axisymmetric notch having the dimensional properties summarised in Table 2 was considered initially in order to assess the suitability of the finite element mesh. The dimensions of the notch were selected to coincide as closely as possible with one of the notches considered in the seminal work of Alleyne et al. (1998).

Eight node, quadratic axisymmetric finite elements (Cook, 1981) are utilized in the present simulations for the finite element region around the notch. For simplicity, a uniform idealization is

[13] A quantity embellished with a superscript asterisk indicates that it is a normalization which is dimensionless.

Table 2
Dimensions of the outer surface breaking, axisymmetric notch.

Property	Assigned value
Depth of notch, d, mm	2.79
Axial length of notch, l, mm	3.17
Depth to wall thickness ratio, (d/H)	0.500
Axial length to wall thickness ratio, (l/H)	0.568

selected. After transparency checks, convergence is assessed by considering different mesh configurations. The suitability of the axial discretization is assessed by considering mesh configurations having one, two, or four finite elements in the axial direction. Similarly checks on the radial discretization were performed using meshes having twenty (ten), ten (five), six (three), or four (two) finite elements in the radial direction for the wave function (finite element) region, respectively. The process and results are detailed in Stoyko (2012).

The sensitivity of the computed scattered wave amplitudes to various meshes is gauged by comparing the reflection coefficients,[14] evaluated at 70 kHz, of various single modes incident on the notch described by the parameters given in Table 2. Only the reflection component corresponding to the incident mode is considered for the L(0,1), F(10,1), and L(0,2) modes examined. The first two modes are selected on the basis that they have the smallest wavelengths in the axial and circumferential directions, respectively, of any of the waves that propagate at 70 kHz. On the other hand, the L(0,2) mode is selected on the basis that experimental data is available (Alleyne et al., 1998). As an example, the resulting magnitudes of the reflection coefficient for the L(0,2) mode changes by less than 1% for the various meshes. Hence the magnitude is essentially independent of the different finite element meshes investigated. Similar results are seen for the L(0,1) and F(10,1) modes.

Ultimately, a finite element region having ten (five) finite elements is used to describe the behavior over the wall thickness in the wave function (finite element) region. Furthermore, four finite elements, which together correspond to half the notch's axial extent, are utilized axially. This selection allows longer axial notches to be represented without the need for additional axial finite elements. Note that the smallest propagating wavelength over the excitation's bandwidth is about $3.4H$, and belongs to the L(0,1) mode. Consequently, the ratio of the smallest (axial) wavelength excited to a finite element's axial length is approximately 48, almost five times larger than the (minimum) recommended guideline given by Alleyne et al. (1998) of ten elements per shortest wavelength. Furthermore, the spatial aspect ratio (i.e., the ratio of the finite elements' dimensions in the radial and axial directions) was approximately 1.4 which is near the desirable value of 1.0. Therefore, each finite element is quite "compact" and likely to behave reasonably (Cook, 1981).

Predictions made with the use of the axisymmetric program are corroborated next by employing available, but limited, experimental data. A very brief description of the methodology used in the seminal work of Alleyne et al. (1998) is given first. Then reflection coefficients predicted using the hybrid SAFE and standard finite element procedure are compared with the data given in Alleyne et al. (1998) are compared for axisymmetric notches.

A specially designed "ring" transducer, described in Alleyne and Cawley (1996), is utilized in Alleyne et al. (1998) to induce an essentially axisymmetric force applied axially on the pipe's outer surface to produce principally longitudinal wave modes. To establish a "base case," a transient excitation is applied to the ring transducer and the reflection from the free end of a pipe is measured. Then the procedure is repeated to measure the separate reflections from a series of individual notches. The invariant temporal form of the excitation is similar to the one described in Section 3.3. It has the same general form and center frequency but with a slightly narrower, 60 kHz to 85 kHz or so, frequency bandwidth as ten rather than seven temporal cycles are used. The only propagating longitudinal modes generated in this bandwidth are L(0,1) and L(0,2). A modest distance between the transducer's location and the pipe's end permits individual end reflections from these two modes to be distinguished as a consequence of their distinct arrival times at the receiving cross section. Moreover, there are virtually no interactions at the measurement location between the incident and reflected waves. The amplitude of the end reflection[15] of the L(0,2) mode is employed as a reference for the "strength" of this mode's reflection from various notches. The ratio, at a given location, of the reflection amplitude from a notch to that of the free end reflection is taken to be the reflection coefficient for the L(0,2) mode.[16] This particular mode is selected because it (i) has the largest group wavespeed, and (ii) is essentially nondispersive over the frequency bandwidth employed. Consequently the displacement responses created by the L(0,2) mode can be identified straightforwardly. In addition to experimental data, Alleyne et al. (1998) give numerical results from an axisymmetric finite element model.

Fig. 4 compares the present and published (Alleyne et al., 1998) reflection coefficient, $|R_{L(0,2),L(0,2)}|$, for axisymmetric notches. A comprehensive assessment of such a notch's axial extent is provided in addition to confirming previously noted effects of different excitation frequencies as well as an axisymmetric notch's depth. Each parameter is varied individually in a given subfigure with the remaining parameters kept at constant reference values. The reference depth and axial length are presented in Table 2 and the reference frequency is 70 kHz. Fig. 4(a) shows that the predicted and experimental reflection coefficients found by different authors is invariably within a reasonable 13%. The earlier finite element result lies approximately midway between the current prediction and the previous measurements. Plausible suggestions for this difference include a slightly varying pipe wall thickness and a possible error in the measured, reference end reflection[17] (Alleyne et al., 1998). On the other hand, the somewhat higher reflection coefficient predicted here could stem, in part, from the fewer (six) and lower order (linear) stiffer elements used in Alleyne et al. (1998). Another contributing factor could arise from an ambiguous axial extent of the notch. It was suggested to be 1.6 mm for the finite element analysis but a 3.2 mm diameter, "slot drill cutter" was used for its machining. This difference is unimportant if the notch's axial length is insignificant. To further assess the discrepancy, an axisymmetric notch was simulated that had the same depth but one-half the axial length of the notch described in Table 2. The calculated L(0,2) reflection coefficient was reduced from 0.41 to 0.36 which agrees very well with the value of 0.37 given in Alleyne et al. (1998) for their simulation. Indeed, the reflection coefficient for the L(0,2) and, later, the T(0,1) mode were found to be "sensitive to the axial extent of a part-through but not a through-wall notch" (Alleyne et al., 1998; Demma et al., 2004). It is seen again that $|R_{L(0,2),L(0,2)}|$ is (i) a weak function of the excitation frequency over the given bandwidth, and (ii) a stronger function of the axisymmetric notch's depth for the 70 kHz excitation. Although the corresponding trend for different axial lengths is more modest than that for the depth, the changes are not negligible.

[14] The reflection and transmission coefficients are complex numbers. However, only the corresponding magnitudes are given usually.

[15] The L(0,2) mode is reflected perfectly at a free end.

[16] The only reflection coefficient considered in Alleyne et al. (1998) is that of the L(0,2) mode when it is incident and scattered alone, i.e., $R_{L(0,2),L(0,2)}$. When comparisons are made later to Alleyne et al. (1998) $R_{L(0,2),L(0,2)}$ is termed "the reflection coefficient of the L(0,2) mode".

[17] This comment is expanded upon in Stoyko (2012).

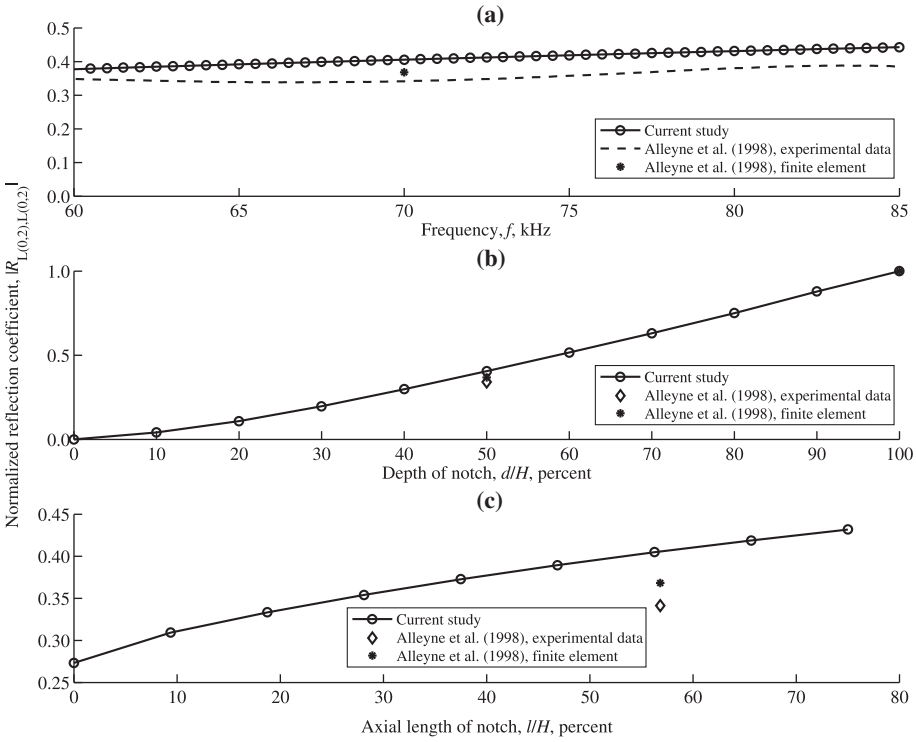

Fig. 4. Magnitude of the reflection coefficient, $|R_{L(0,2),L(0,2)}|$, for various (a) excitation frequencies and axisymmetric notches having different (b) depths, and (c) axial lengths.

Having compared the predictions to available experimental data, excitations that excite a plethora of coexisting modes are simulated. A transient point-like force is applied radially to the simulated pipe's outer surface. It has the temporal form shown in Fig. 3 and is positioned at $z_L^* = (z_L/H) = 5.1$, where z_L is the transmitting transducer's axial coordinate.[18] The resulting radial displacement is computed on the pipe's outer surface at $\theta_R = 0$, i.e., a pure axial offset from the point load, and $z_R^* = (z_R/H) = 10.2$, where z_R is the axial coordinate of the receiving transducer located in the reflected field.[19] All pertinent positions are shown in Fig. 1.

As stated earlier, the (approximate) wave functions for the undamaged pipe were determined by using SAFE. Then the hybrid-SAFE technique was applied on a mode by mode and frequency by frequency basis. A modal superposition was applied at each frequency and the inverse Fourier transform was approximated using a numerical integration scheme to recover time histories from the approximate spectral densities. Fig. 5 shows the displacement responses predicted in time and frequency for a pipe having no notch and a pipe having the outer surface breaking notch with the dimensions given in Table 2. The displacement responses are evaluated on the pipe's outer surface where $\theta_R = 0$ and $z_R^* = (z_R/H) = 10.2$.

A cursory examination of Fig. 5 shows that the incident and reflected waves interact and cannot be separated in time. However, the notch's presence is discerned easily from a comparison of the corresponding spectral densities. This is because each predominant peak in the spectral density of Fig. 5(b) "splits" into two local maxima in Fig. 5(d), one on either side of the original peak. The sharper maximum at the lower frequency also has a much large amplitude so, for convenience, it is termed a "singularity." Differences between the frequencies of such singularities and the nearest cutoff behavior of the undamaged pipe, having the frequencies shown in Fig. 5(b) are presented in Table 3.

The behavior seen in Fig. 5(d) is illustrated more clearly in Fig. 6 for the pipe's F($\pm$10, 1) modes. The frequency scale in this figure is expanded about the undamaged pipe's F($\pm$10, 1) modes' cutoff frequencies. The latter, as well as the singularity introduced by the notch are indicated in this figure. It is clear that the singularity does not coincide with the undamaged pipe's F($\pm$10, 1) modes' cutoff frequencies.

To help explain the frequency dependent behavior of the notched pipe in the neighborhood of the undamaged pipe's cutoff frequencies, Fig. 7 shows other normalized reflection coefficients predicted for the flexural F(n, 1) modes, where n equals 8 through 13, for an axisymmetric notch having $(d/H) = 0.500$ and $(l/H) = 0.568$. Each curve represents a single F(n, 1) mode which is reflected into itself. (Modal conversions from F(n, 1) into F(n, m), $m \neq 1$, are not given for brevity. Such conversions are required, however, to satisfy continuity and boundary conditions. They are modeled by the procedure used to produce Fig. 7.) For easier comparisons, the frequency axis in Fig. 7 has been normalized by the cutoff frequency of the mode in question and expanded to lower frequency ratios. It is noteworthy now that each curve can be seen to possess two singularities. The singularity near a normalized frequency of 1.0 occurs, as before, at a frequency just below the undamaged pipe's relevant cutoff frequency. This observation can be corroborated by noting that the normalized reflection coefficients always pass through the point (1.0, 1.0) for these modes. On the other hand, the singularity around the lower normalized frequency of 0.7 always corresponds to a mode transitioning from evanescent to non-propagating. The practical usefulness of this singularity, however, may be limited. Waves scattered from the axisymmetric notch at frequencies near this singularity decay exponentially from the notch's vertical boundaries at a rate of about $\exp(-z_d^*)$. The z_d^* is the distance from the notch's boundary, normalized by the undamaged pipe's thickness, H. The decay rate in the axial direction is determined approximately based on the

[18] Note that angles are measured relative to the idealized force's central point of application.

[19] The transmitted and reflected fields give similar information so the former is omitted.

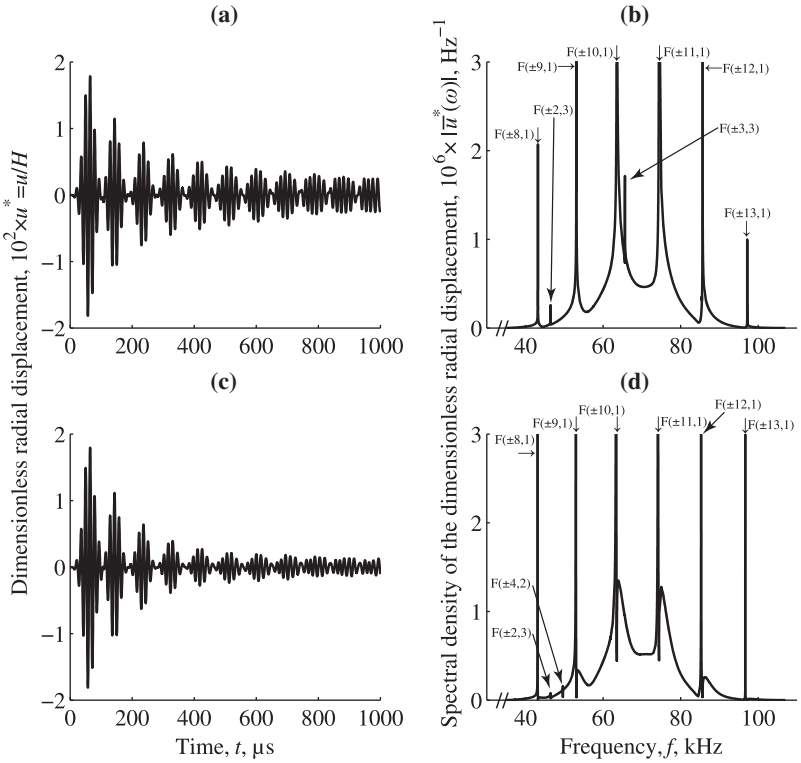

Fig. 5. Radial displacement predicted on the pipe's outer surface within the reflected field where $\theta_R = 0$ and $z_R^* = (z_R/H) = 10.2$ for an axisymmetric notch having $(d/H) = 0.500$ and $(l/H) = 0.568$. Sub-figures (a) and (b) ((c) and (d)) give the direct (superposition of direct and reflected) waves produced by a radial point force.

Table 3
Frequencies that correspond to the readily identified singularities appearing in Fig. 5(d). They are distinct from the undamaged pipe's cutoff frequencies.

Circumferential wavenumber, n	Axial order, m	Frequency of singularity (kHz)	Difference between cutoff and singularity frequency (kHz)
±8	1	43.112	0.085
±2	3	46.462	0.001
±4	2	49.623	0.294
±9	1	52.983	0.129
±10	1	63.362	0.192
±11	1	74.153	0.273
±12	1	85.274	0.377
±13	1	96.660	0.503

behavior of the representative F(10,1) mode's axial wavenumber found from Fig. 8. The latter figure shows that the imaginary part of the dimensionless axial wavenumber of this mode is almost one when the mode transitions from evanescent to nonpropagating. The quite large exponent suggests that the effect is very localized and likely to be masked by the propagating modes. The singularity just below the cutoff frequency of 63.553 kHz, on the other hand, is more interesting. Its effect is not so localized because the magnitude of the imaginary part of its wavenumber is much closer to zero. Indeed, another "back of an envelope" calculation[20] based on Fig. 8 suggests that the axial decay rate is about $\exp(-0.15z_d^*)$ at the notch-induced singularity. As a consequence of the smaller exponent, this last singularity may be detectable to about $10H$ or 5 cm from the axisymmetric notch's vertical boundaries.

[20] This calculation plausibly assumes that the spectral density's amplitude at the higher frequency singularity is at least four times greater than that at the "plateau" or "null."

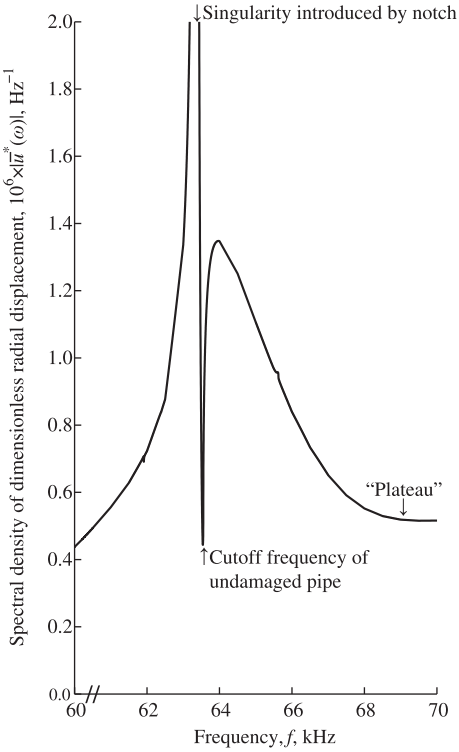

Fig. 6. Spectral density on the pipe's outer surface in the reflected field where $\theta_R = 0$ and $z_R^* = (z_R/H) = 10.2$ for an axisymmetric notch having $(d/H) = 0.500$ and $(l/H) = 0.568$. The frequency scale is enlarged about the undamaged pipe's F(±10,1) modes' cutoff frequencies.

An analysis of the eigenvalues (resonant frequencies) of solely the finite element region (which can be found in Stoyko (2012)) indicates that the frequency of the possibly more important singu-

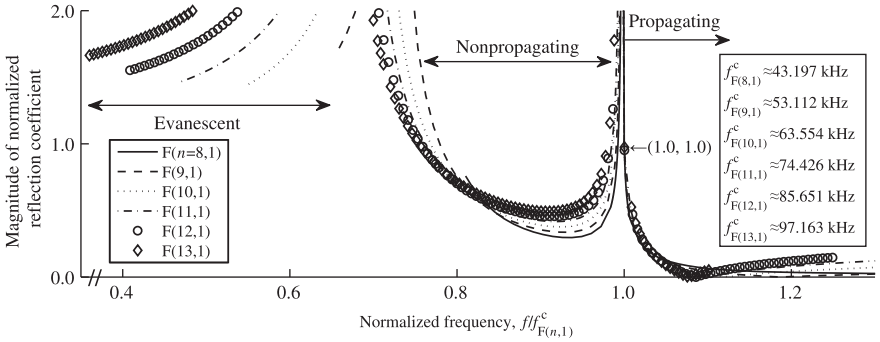

Fig. 7. Normalized reflection coefficient caused by flexural $F(n,1)$ modes, where n is 8 through 13 inclusive, and an axisymmetric notch having $(d/H) = 0.500$ and $(l/H) = 0.568$. The $f^c_{F(n,1)}$ is the cutoff frequency of the undamaged pipe's $F(n,1)$ mode.

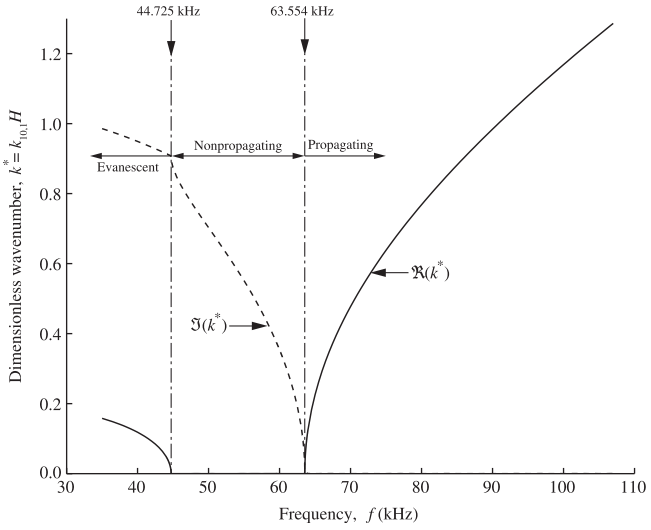

Fig. 8. Real and imaginary parts of the undamaged pipe's F(10,1) dimensionless axial wavenumber, $k^* = k_{10,1}H$ as a function of frequency.

larity does not correspond to a resonant frequency of the finite element region alone. It depends presumably upon the properties of *both* the finite element region and the wave function expansion regions. Moreover, the last column of Table 3 shows that the difference between the frequency of this singularity and the corresponding undamaged pipe's cutoff frequency grows continuously as the circumferential wavenumber increases. Advantage might be taken of this trend by increasing the center frequency of the point force to excite modes having larger circumferential wavenumbers in order to make the frequency differences easier to measure.

Having examined the wave scattering from one particular notch, wave scattering by axisymmetric notches having various dimensions was modeled by using the finite element idealization described previously. Fig. 9 presents the frequency difference (reduction), Δf, from a nearby cutoff frequency of the undamaged pipe caused by each notch. Results are shown for the representative F(10,1) mode. Frequency reductions can be seen to depend upon an axisymmetric notch's depth and, to a less degree, its axial length. To determine these two dimensions, constant frequency differences are projected for each of the F(10,1), F(11), and F(12,1) modes onto their common horizontal plane. These projections are superimposed in Fig. 10. Not surprisingly it can be seen that, due to the contours' "U-shapes," the depth ratio of a notch for a given axial length ratio, (l/H), and constant frequency reduction, Δf, cannot be found absolutely from any single one of the three modes. Consequently more than one mode has to be employed – a situation which is common to a reflection based procedure (Demma et al., 2004).

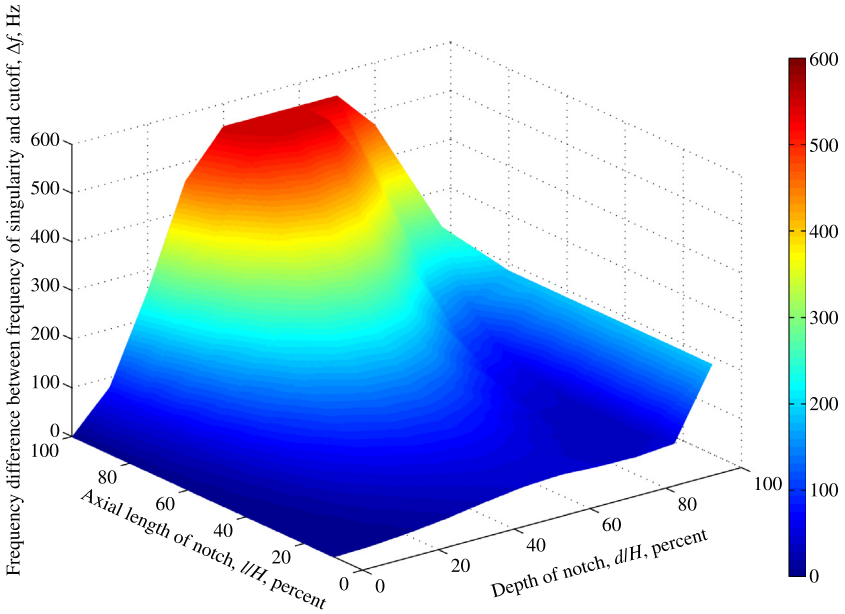

Fig. 9. Frequency differences, Δf, from the undamaged pipe's F(10,1) cutoff frequency introduced by axisymmetric notches having various dimensions.

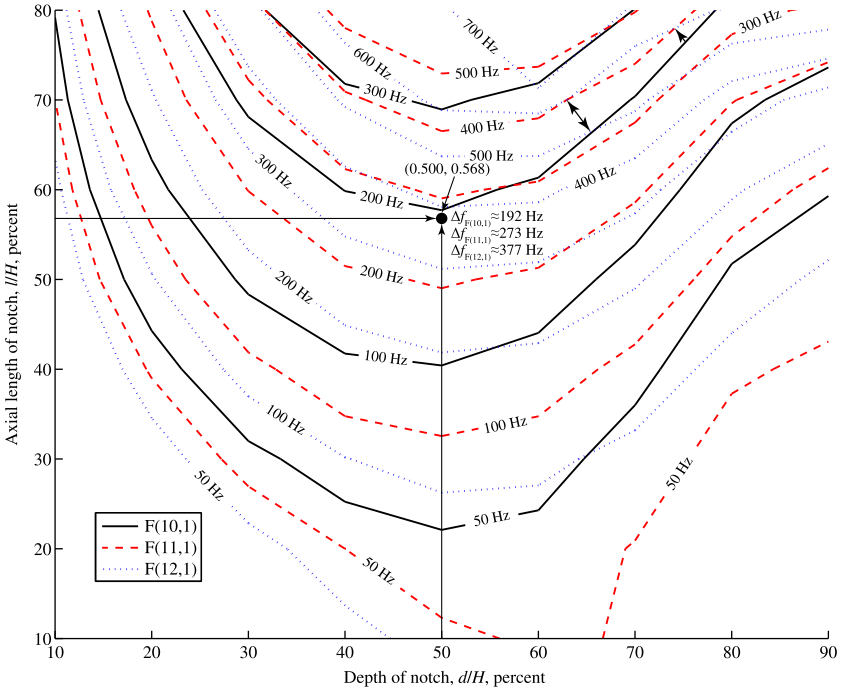

Fig. 10. Contour maps of constant frequency differences between the singularity produced by an axisymmetric notch and the undamaged pipe's cutoff frequencies for the F(10,1), F(11,1), and F(12,1) modes. The solid (dashed) {dotted} curves correspond to contours of the F(10,1) [F(11,1)] {F(12,1)} mode.

The intersection of the contours of two different flexural modes is usually unique. See, for example, the 200 Hz and 300 Hz contours for the F(11,1) and F(12,1) modes, respectively. The single intersection of the contours provides two coordinates which uniquely define the two dimensions of an axisymmetric notch. Interpolations are obviously needed if a frequency difference does not lie precisely on a contour line. An example of this situation is illustrated in Fig. 10 where the frequency differences tabulated in Table 3 for the F(10,1), F(11,1), and F(12,1) modes are indicated. These differences can be used to uniquely characterize the notch's dimensions. Fig. 10 also suggests that, for a given frequency difference, a flexural mode with a higher circumferential wavenumber has a lower position. Consequently such modes are more sensitive to smaller notches. There are instances, however, when the curves for two different modes intersect more than once. One such example seen in Fig. 10 occurs for the 400 Hz and 600 Hz contours of the F(11,1) and F(12,1) modes, respectively. In this instance the two arrowed distances from the F(10,1) mode's 200 Hz reference contour may be used to distinguish the two intersections. Then, by interpolating linearly between the 200 Hz and 300 Hz contours of the F(10,1) mode, a frequency difference in the F(10,1) mode of around 225 Hz would suggest a notch having $(d/H) \approx 0.73$ and $(l/H) \approx 0.78$. On the other hand, a frequency difference of about 260 Hz in the F(10,1) mode would imply a notch with $(d/H) \approx 0.62$ and $(l/H) \approx 0.70$. Clearly, however, each additional intersection requires knowledge of another mode's frequency difference to uniquely determine a notch's dimensions. Furthermore, an excitation such as a point force which simultaneously excites several modes becomes more advantageous as the number of required modes increases.

3.6. Nonaxisymmetric notch

The extension to nonaxisymmetric notches is considered now. Only the introduction of singularities distinct from the cutoff frequencies by a nonaxisymmetric notch will be demonstrated here, i.e., no parameter study is undertaken for the nonaxisymmetric case. This apparent neglect is because the computational burden associated with the three-dimensional finite elements used in the nonaxisymmetric case precludes such a parameter study at this time.

Twenty-seven node, brick finite elements using quadratic Lagrange interpolation polynomials in each coordinate direction (Cook, 1981) were employed for the finite element region around the notch. The notch was modeled again by simply removing finite elements. As in the axisymmetric case, the singularities (in the stress field) at the notch's corners are not described accurately by this method, which limits the accuracy of the stresses in the near field. The far field behavior is modeled, however, with sufficient accuracy to be meaningful. Ultimately, ten (five) finite elements described the behavior over the full (half) wall thickness. To reduce computer waiting time, the minimally acceptable two finite elements represented the notch's axial extent. However, 126 elements were deployed around the pipe's circumference. The radial discretization of ten elements through the pipe's wall was selected so that the wavefunctions from the previous axisymmetric analysis could be employed.

The appropriateness of the minimal axial discretization was checked by simulating the axisymmetric notch described in Section 3.5 with the three-dimensional software. A comparison of the two sets of reflection and transmission coefficients showed that they were essentially indistinguishable. The circumferential discretization was determined, after selecting the radial and axial discretizations, by considering the results from transparency tests. The number of finite elements around the undamaged pipe's circumference was increased gradually until the reflection coefficient was less than 0.01 for all the modes propagating over some part of the excitation's bandwidth (Stoyko, 2012). Therefore any reflection coefficient which has a magnitude greater than 0.01 for a propagating mode has an inconsequential error from this modeling component. Not surprisingly, the F(13,1) mode dictated the circumferential discretization as it has the smallest $(3.6H)$ circumferential wavelength of the propagating modes. On the other hand, the propagating L(0,1) mode has a somewhat smaller axial

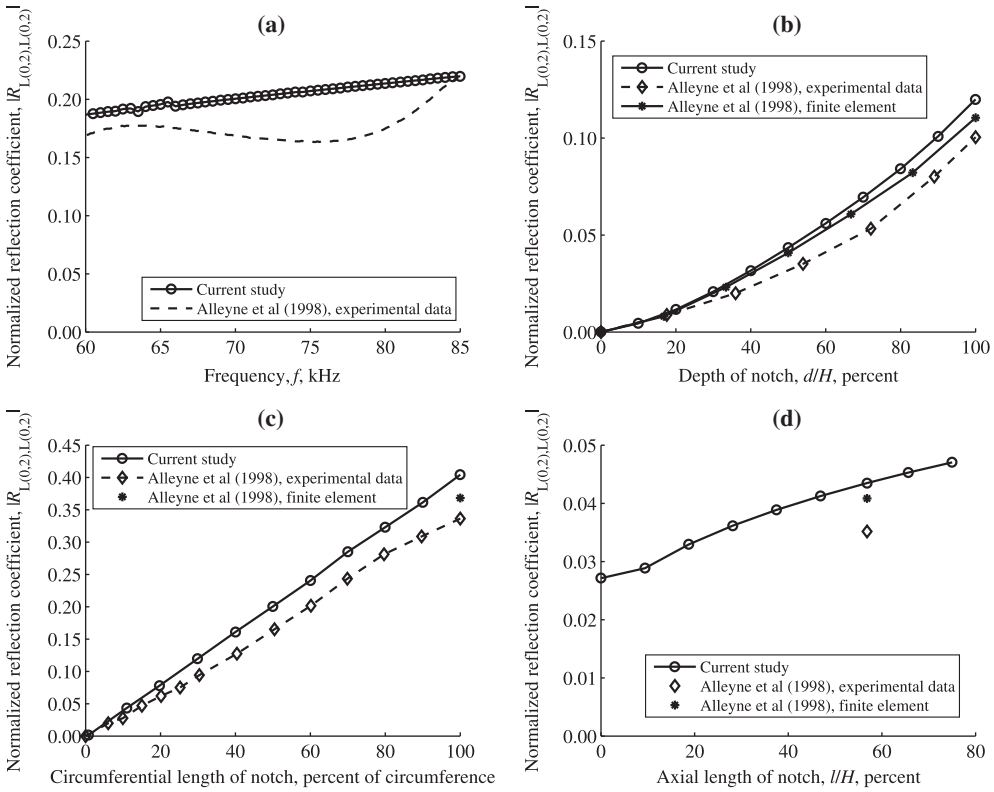

Fig. 11. Magnitude of the normalized reflection coefficient, $|R_{L(0,2),L(0,2)}|$, for different (a) excitation frequencies, (b) depths, (c) circumferential extents, and (d) axial lengths of nonaxisymmetric notches.

wavelength of around 3.4*H*. Consequently, the ratio of the smallest axial wavelength of all the propagating modes to a finite element's axial length was approximately 12 – a value which is above the recommended lower bound of ten elements per shortest wavelength (Alleyne et al., 1998). Similarly, the ratio of the F(13,1) mode's (circumferential) wavelength to a finite element's circumferential length was virtually 10. Moreover, the spatial aspect ratios (i.e., the ratios of the finite elements' lengths in the axial and circumferential directions to those in the radial direction) were approximately in the proportions of 2.4 to 0.4 to 1.0 which, experience suggests, is near the desirable value of 1.0. Hence each finite element is reasonably "compact" and likely to behave well (Cook, 1981).

As in the axisymmetric case, comparisons were made with the results published in Alleyne et al. (1998). Fig. 11 compares present and published (Alleyne et al., 1998) reflection coefficients, $|R_{L(0.2),L(0.2)}|$, for nonaxisymmetric notches.[21] A more complete assessment of the effect of such a notch's axial extent is provided in addition to confirming previously published results. The format and reference values employed in the development of Fig. 4 for the axisymmetric notches are retained. However, a nonaxisymmetric notch no longer extends completely around the pipe's circumference. The half (or 50%) circumferential notch considered in Fig. 11(a) is reduced to 11% in Fig. 11(b) and (d), so that direct comparisons can be made with Alleyne et al. (1998). Previous observations based upon Fig. 4 still apply.

The procedure for the nonaxisymmetric notch is essentially the same as that followed previously for the axisymmetric case. Fig. 12 shows the normalized reflection coefficients of the modes $n \geqslant 0$ that propagate over at least some portion of the excitation's 35 kHz to 107 kHz bandwidth for the F(13,1) mode incident on a nonaxisymmetric notch. Only the F(10,1), F(11,1), F(12,1), F(13,1) modes participate significantly. On the other hand, "cross-coupling" exists now between modes having different circumferential wavenumbers. This notch has the same depth and axial extent as the axisymmetric notch considered earlier (see Table 2) but the circumferential extent is reduced to one-half the pipe's circumference. This notch is considered because experimental and finite element data are available for comparisons.

A singularity occurring between 97.00 kHz and 97.05 kHz is seen in the reflection coefficients shown in Fig. 12. The F(10,1), F(12,1), and F(13,1) modes are observed to be noticeably reflected in this frequency range by the incident F(13,1) mode. The frequencies of the scattered waves' singularities caused by the nonaxisymmetric notch's introduction do not coincide again with the undamaged pipe's cutoff frequencies, the nearest being the F(13,1) mode's cutoff frequency of 97.164 kHz, which is found from the SAFE model. Conclusions derived from axisymmetric notches generally extend straightforwardly to nonaxisymmetric notches. Therefore it should be possible, in principle, to use analogous frequency differences introduced by a nonaxisymmetic notch to estimate its dimensions. However, additional modes and, hence, frequency differences are most likely needed. Computational requirements could be made less onerous if advantage is taken of the need for only frequency information rather than a complete solution of the linear equations describing the wave scattering problem.

4. Conclusions and closing remarks

A hybrid SAFE and standard finite element procedure was applied to detect and characterize an open notch in an infinitely

[21] The finite element results given in Alleyne et al. (1998) are extrapolated by multiplying each result from a corresponding axisymmetric notch by the percentage ratio of the part circumferential notch length to the pipe's total circumference.

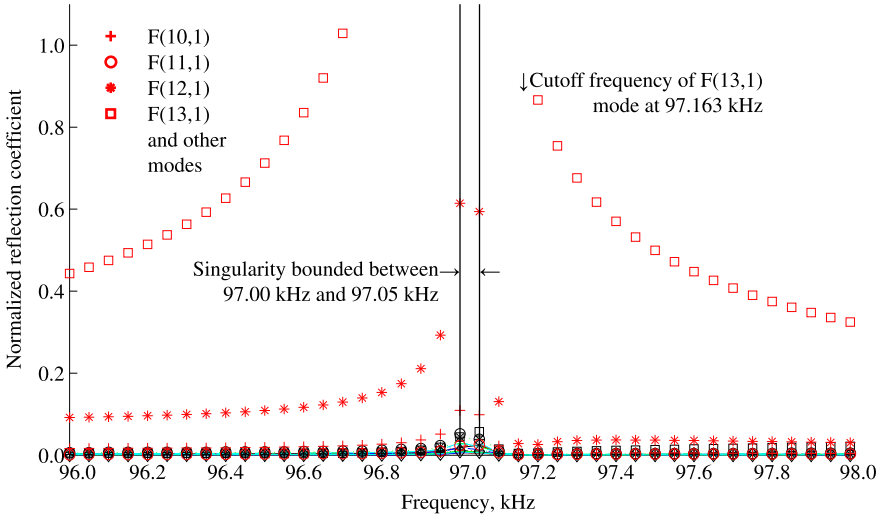

Fig. 12. Showing selected normalized reflection coefficients for the F(13,1) mode incident.

long steel pipe. Axisymmetric notches were considered first. Interactions between incident as well as dispersive guided waves and the axisymmetric notch were shown numerically to change a radial displacement's temporal history and introduce additional, singularity-like information in the previously undamaged pipe's Frequency Response Function (FRF). This information indicated the presence of a nearby notch. Moreover, frequency differences between the "singularities" of the undamaged and damaged pipes were shown to reflect an axisymmetric notch's dimensions. A procedure by which an axisymmetric notch's dimensions could be estimated was demonstrated by considering the frequency differences for multiple modes. It is envisioned that, in practice, the experimental and signal processing techniques described in Stoyko et al. (2010) could be utilized to simultaneously excite several modes and measure the resulting singularity frequencies. The extension to nonaxisymmetric notches was suggested.

The frequency differences are seen to grow with a larger circumferential wavenumber. Advantageous use might be made of this property by increasing the center frequency of the excitation in order to excite modes having higher circumferential wavenumbers. Effects are localized around the notch's axial boundaries, however, because the frequencies at which additional singularities occur are below nearby cut-off frequencies. This localization might be expected to become more severe with an increasing circumferential wavenumber as a result of correspondingly increasing frequency differences. Because the technique applies only locally it is unsuitable for rapidly screening large sections of pipe, unlike other complementary methods. While no new experimental data is given, preliminary experiments have shown that introducing a notch in a pipe generates singularities distinct from the pipe's cut-off frequencies. However, only "sharp," rectangular notches are considered. The extension to notches having different geometries (Zhu, 2002) still needs to be examined. Notwithstanding, the hybrid-SAFE approach can be applied straightforwardly to *any* arbitrary geometry providing that a finite element mesh suitably represents a notch's geometry.

Acknowledgments

All three authors acknowledge the financial support from the Natural Science and Engineering Research Council (NSERC) of Canada. The first author also wishes to acknowledge financial aid from the University of Manitoba Students' Union (UMSU), Society of Automotive Engineers (SAE) International, University of Manitoba, Province of Manitoba, and Ms. A. Toporeck and family. The Wawanesa Mutual Insurance Company is thanked for their generous donation of goods in kind. The authors wish also to thank Dr. Joseph L. Rose, Paul Morrow Professor of Engineering Design and Manufacturing, of the Pennsylvania State University for the useful suggestions he made as the external examiner for the first author's doctoral dissertation. The experimental efforts of Mr. Kazeem Adeogun are recognized.

References

Alberta Energy and Utilities Board, 2007. Pipeline performance in Alberta, 1990–2005. Tech. Rep. 2007-A, Alberta Energy and Utilities Board, Calgary, Alberta, Canada. <http://www.ercb.ca/docs/Documents/reports/r2007-A.pdf>.

Alleyne, D.N., Cawley, P., 1996. Excitation of Lamb waves in pipes using dry-coupled piezoelectric transducers. J. Nondestr. Eval. 15, 11–20.

Alleyne, D.N., Lowe, M.J.S., Cawley, P., 1998. Reflection of guided waves from circumferential notches in pipes. J. Appl. Mech. 65 (3), 635–641.

Alleyne, D.N., Pavlakovic, B., Lowe, M.J.S., Cawley, P., 2001. Rapid, long range inspection of chemical plant pipework using guided waves. In: Thompson, D., Chimenti, D., Poore, L. (Eds.), Review of Progress in Quantitative Nondestructive Evaluation, American Institute of Physics, vol. 20. Melville, New York, pp. 180–187.

Andersen, T., Misund, A., 1983. Pipeline reliability: an investigation of pipeline failure characteristics and analysis of pipeline failure rates for submarine and cross-country pipelines. J. Pet. Technol. 35 (4), 709–717.

Bai, H., Chitikireddy, R., Shah, A.H., Datta, S.K., 2011. Generalized thermoelastic waves in cylinders due to localized heating. J. Mech. Mater. Struct. 6 (1–4), 31–50.

Bai, H., Shah, A.H., Popplewell, N., Datta, S.K., 2001. Scattering of guided waves by circumferential cracks in steel pipes. J. Appl. Mech. 68 (4), 619–631.

Bai, H., Taciroglu, E., Dong, S.B., Shah, A.H., 2004. Elastodynamic Green's functions for a laminated piezoelectric cylinder. Int. J. Solids Struct. 41 (22–23), 6335–6350.

Benmeddour, F., Treyssède, F., Laguerre, L., 2011. Numerical modeling of guided wave interaction with non-axisymmetric cracks in elastic cylinders. Int. J. Solids Struct. 48 (5), 764–774.

Cawley, P., Lowe, M.J.S., Simonetti, F., Chevalier, C., Roosenbrand, A., 2002. The variation of the reflection coefficient of extensional guided waves in pipes from defects as a function of defect depth, axial extent, circumferential extent and frequency. Proc. Inst. Mech. Eng., Part C: J. Mech. Eng. Sci. 216 (11), 1131–1144.

Chitikireddy, R., Datta, S.K., Shah, A.H., Bai, H., 2011. Transient thermoelastic waves in an anisotropic hollow cylinder due to localized heating. Int. J. Solids Struct. 48 (21), 3063–3074.

Cook, R., 1981. Concepts and Applications of Finite Element Analysis, second ed. John Wiley and Sons, New York, NY, USA.

Demma, A., Cawley, P., Lowe, M.J.S., Roosenbrand, A.G., Pavlakovic, B., 2004. The reflection of guided waves from notches in pipes: a guide for interpreting corrosion measurements. NDT E Int. 37 (3), 167–180 <http://dx.doi.org/10.1016/j.ndteint.2003.09.004>.

Hay, T., Rose, J., 2002. Flexible PVDF comb transducers for excitation of axisymmetric guided waves in pipe. Sens. Actuators A: Phys. A100 (1), 18–23.

Huang, C.H., Dong, S.B., 2001a. Analysis of laminated circular cylinders of materials with the most general form of cylindrical anisotropy I. Axially symmetric deformations. Int. J. Solids Struct. 38 (34–35), 6163–6182.
Huang, C.H., Dong, S.B., 2001b. Analysis of laminated circular cylinders of materials with the most general form of cylindrical anisotropy. II: Flexural deformations. Int. J. Solids Struct. 38 (34–35), 6183–6205.
Huang, K.H., Dong, S.B., 1984. Propagating waves and edge vibrations in anisotropic composite cylinders. J. Sound Vib. 96 (3), 363–379.
Krautkrämer, J., Krautkrämer, H., 1977. Ultrasonic Testing of Materials, second ed. Springer-Verlag, Berlin, Germany.
Li, J., Rose, J.L., 2001. Excitation and propagation of non-axisymmetric guided waves in a hollow cylinder. J. Acoust. Soc. Am. 109 (2), 457–464.
Ma, J., Simonetti, F., Lowe, M.J.S., 2006. Scattering of the fundamental torsional mode by an axisymmetric layer inside a pipe. J. Acoust. Soc. Am. 120 (4), 1871–1880.
Mahmoud, A., Shah, A.H., Popplewell, N., 2004. Parallel hybrid algorithm for three-dimensional elastic wave scattering in steel pipes. Trans. ASME J. Pressure Vessel Technol. 126 (4), 510–517.
Marzani, A., 2008. Time-transient response for ultrasonic guided waves propagating in damped cylinders. Int. J. Solids Struct. 45 (25–26), 6347–6368.
Mohr, W., Hoeller, P., 1976. On inspection of thin-walled tubes for transverse and longitudinal flaws by guided ultrasonic waves. IEEE Trans. Sonics Ultrason. SU-23 (5), 369–374.
Mu, J., Zhang, L., Rose, J.L., 2007. Defect circumferential sizing by using long range ultrasonic guided wave focusing techniques in pipe. Nondest. Test. Eval. 22 (4), 239–253.
Nelson, R.B., Dong, S.B., Kalra, R.D., 1971. Vibrations and waves in laminated orthotropic circular cylinders. J. Sound Vib. 18 (3), 429–444.
Oliver, J., 1957. Elastic wave dispersion in a cylindrical rod by a wide-band short-duration pulse technique. J. Acoust. Soc. Am. 29 (2), 189–195.
Owen, D.R.J., Fawkes, A.J., 1983. Engineering Fracture Mechanics: Numerical Methods and Applications. Pineridge Press, Swansea, UK.
Rattanawangcharoen, N., Shah, A.H., Datta, S.K., 1992. Wave propagation in laminated composite circular cylinders. Int. J. Solids Struct. 29 (6), 767–781.
Rattanawangcharoen, N., Zhuang, W., Shah, A.H., Datta, S.K., 1997. Axisymmetric guided waves in jointed laminated cylinders. J. Eng. Mech. 123 (10), 1020–1026.
Rose, J.L., Barshinger, J.N., 1998. Using ultrasonic guided wave mode cutoff for corrosion detection and classification. Proc. IEEE Ultrason. Symp. 1, 851–854.
Rose, J.L., Jiao, D., Spanner Jr., J., 1996. Ultrasonic guided wave NDE for piping. Mater. Eval. 54 (11), 1310–1313.
Rose, J.L., Quarry, M., 1999. Feasibility of ultrasonic guided waves for non-destructive evaluation of gas pipelines. Tech. Rep. GRI-99/0076, Gas Research Institute, Chicago, IL, USA.
Rose, J.L., Sun, Z., Mudge, P.J., Avioli, M.J., 2003. Guided wave flexural mode tuning and focusing for pipe testing. Mater. Eval. 61 (2), 162–167.
Shin, H.J., Rose, J.L., 1998. Guided wave tuning principles for defect detection in tubing. J. Nondestr. Eval. 17 (1), 27–36.
Shin, H.J., Rose, J.L., 1999. Guided waves by axisymmetric and non-axisymmetric surface loading on hollow cylinders. Ultrasonics 37 (5), 355–363.
Silk, M., Bainton, K., 1979. Propagation in metal tubing of ultrasonic wave modes equivalent to Lamb waves. Ultrasonics 17, 11–19.
Silva, M.Z., Gouyon, R., Lepoutre, F., 2003. Hidden corrosion detection in aircraft aluminum structures using laser ultrasonics and wavelet transform signal analysis. Ultrasonics 41 (4), 301–305.
Stoyko, D.K., 2005. Interpreting Wave Propagation in a Homogeneous, Isotropic, Steel Cylinder (Master's thesis). University of Manitoba. <http://hdl.handle.net/1993/97>.
Stoyko, D.K., 2012. Using the Singularity Frequencies of Guided Waves to Obtain a Pipe's Properties and Detect and Size Notches (Ph.D. thesis). University of Manitoba. <http://hdl.handle.net/1993/9818>.
Stoyko, D.K., Popplewell, N., Shah, A.H., 2010. Finding a pipe's elastic and dimensional properties using ultrasonic guided wave cut-off frequencies. NDT E Int. 43 (7), 568–578 <http://dx.doi.org/10.1016/j.ndteint.2010.05.013>.
Zhu, W., 2002. An FEM simulation for guided elastic wave generation and reflection in hollow cylinders with corrosion defects. J. Pressure Vessel Technol. 124 (1), 108–117.
Zhu, W., Rose, J.L., Barshinger, J.N., Agarwala, V., 1998. Ultrasonic guided wave NDT for hidden corrosion detection. Res. Nondestr. Eval. 10 (4), 205–225.
Zhuang, W., Shah, A.H., Datta, S.K., 1997. Axisymmetric guided wave scattering by cracks in welded steel pipes. J. Pressure Vessel Technol. 119 (4), 401–406.
Zhuang, W., Shah, A.H., Dong, S.B., 1999. Elastodynamic Green's function for laminated anisotropic circular cylinders. J. Appl. Mech. 66, 665–674.